A 3D Surface Reconstruction Method Based on Delaunay Triangulation

Wenjuan Miao, Yiguang Liu[✉], Xuelei Shi, Jingming Feng, and Kai Xue

Vision and Image Processing Lab (VIPL), College of Computer Science,
Sichuan University, Chengdu 610065, People's Republic of China
liuyg@scu.edu.cn

Abstract. Point cloud models acquired by passive three-dimensional reconstruction systems based on binocular or multi-view involve large amounts of noise and its distribution is uneven, which affects the accuracy of surface reconstruction. To tackle the problem, we proposed a three-dimensional surface reconstruction method based on Delaunay triangulation. First, use Delaunay triangulation to get a fully adaptive decomposition of point cloud, then the output triangular mesh was represented using dual graph, so by using graph cut optimization the initial surface model was obtained. Second, the deformation model was used to optimize the initial surface model, and then adopted photometric similarity function and Laplace operator to refine surface details. Finally, the refinement was transformed into an iterative procedure, by which the real surface of the object was accurately approximated. We experimented on four standard datasets of Castle-Entry, Castle, Fountain and Herzjesu. The result showed that compared with Poisson surface reconstruction and floating scale surface reconstruction algorithm, the proposed method was more adaptable and robust to noise and outliers, and the detailed information recovery of local surface reconstruction was better. It showed that the method proposed in this paper effectively improved the accuracy and completeness of surface reconstruction, which could reconstruct high quality three-dimensional surface models of object from the point cloud models with lots of noise and complex topological structures.

Keywords: Surface reconstruction · Deformation model · Photometric similarity function

1 Introduction

3D reconstruction technology is widely applied in many fields such as virtual simulation [1,23], non-contact measurement [21], virtual reality [7], battlefield environment perception [4,22], etc. Therefore, it is a significant problem to process 3D point cloud acquired by 3D digital scanning devices, and achieve 3D reconstruction effectively and accurately. In this paper, we focus on processing point cloud to restore the geometry and topology structure of objects. Considering that 3D cloud point acquired by passive 3D reconstruction systems

based on binocular or multi-view involves large amounts of noise and outliers, which affects results of surface reconstruction, we proposed an approach based on Delaunay triangulation. First, Delaunay triangulation was constructed by incremental insertion, after that output triangular mesh was converted into the representation of dual graph, and then we transform the initial surface extraction problem into graph cut optimization. Then due to the loss of details and the roughness of initial surface model, we optimized the initial surface by minimizing the internal and external energy functions of deformation model globally. Finally, surface model was approximated to the real surface of the object through several iterations of all vertices on the surface.

2   Related Work

Surface reconstruction is a major field in computer vision at present. Many surface reconstruction methods is summarized in [2], in this section, we intend to introduce related approaches to our method, including implicit surface reconstruction approaches [5,9,10,20], and surface reconstruction approaches based on Delaunay triangulation [8,11–15].

Kazhdan et al. [9] formulates the surface reconstruction from oriented points as a spatial poisson problem, which suffers a tendency to oversmooth the data. Kazhdan et al. [10] modifies the poisson reconstruction algorithm to add incorporate positional constraints, which improves the geometric surface and detail characteristics of the surface. However, reconstruction results of the approach is easily affected by data redundancy. Fuhrmann et al. [5] achieves surface reconstruction by extracting the zero-level set of the implicit function. Their approach could be extended theoretically, but the interpolation ability of the approach is limited due to the small support area. Wang et al. [20] proposes a surface reconstruction approach based on implicit pht-splines. Their approach could reconstruct high-quality results, but which requires high demand of memory.

The visual hull introduced in [13] is unsuitable for outdoor scene reconstruction because of the dependence on separating object from background. Pan et al. [15] extracts surface by using probabilistic tetrahedron carving algorithm. But their approach is not resistant against outliers and inflexible for the batch processing of data. An approach of multi-view reconstruction is proposed in [12]. They define an energy equation based on visibility information and surface parameters, and minimize this energy by graph cuts [3]. Labatut et al. [11] improves the approach in [12], the photo-consistency is replaced by surface quality term in [11] and smoothing term is combined with a purely discrete visibility term. Their approach has good scalability, but it cannot construct weak-support surface well. Jancosek et al. [8] achieves multi-view reconstruction preserving weakly-supported surfaces which works on [11]. Mostegel et al. [14] proposes a scalable approach of surface reconstruction from 3D multi-scale multi-view stereo point clouds. Their approach extracts surface hypotheses from local Delaunay tetrahedralization and merges overlapping surface hypotheses by graph cuts [3],

finally a consistent mesh is generated. Their approach is resilient to outliers frag-
ments and vast scale changes, but the results of reconstruction is limited by the
localized strategies taken in the original detection process.

3   Initial 3D Surface Reconstruction

In this paper, bundle system [16,17] is adopted to obtain camera parameters
and initial 3D point cloud. The point cloud is processed by PMVS [6], and then
we apply Delaunay triangulation to get a fully adaptive decomposition of point
cloud, which is constructed by incremental insertion. For the initial dense point
cloud, we find the nearest point of the point to be inserted in Delaunay triangu-
lation based on the visibility information of the point, and then the maximum
reprojection error between two 3D points is computed. If the reprojection error
is above threshold e, the point would be inserted in Delaunay triangulation, or
the position of the nearest point would be recomputed. In addition, the visibility
information and confidence information of the nearest point would be updated.
This step outputs a Delaunay triangulation T through traversing all 3D points.

Next we convert the Delaunay tetrahedralization T into the representation of
a dual graph and set weight associated with it. Therefore, the surface is extracted
by performing graph cut optimization on this dual graph. The detailed procedure
is as follows: we assign weights to directed edges of dual graph based on visibility
information and smoothing terms. Accordingly, the minimum cut is extracted by
solving the energy equation as shown in formula (1). S is the initial reconstruction
surface, $E_{visibility}$ is the visibility term, E_{smooth} is the smoothing term and λ is
the weight coefficient. The energy equation is as follows:

$$E(S) = E_{visibility} + \lambda E_{smooth}(S) \tag{1}$$

According to the visibility constraints, all vertices v appearing on the final sur-
face S should not be occluded from the viewpoints b they come from and there-
fore visibility item could be computed as the collision detection problem of the
line-face intersection conflict, as shown in Fig. 1. p_i is a 3D point, c_j is the cen-
ter of camera j. We calculates the intersection of the ray $c_j p_i$ and Delaunay
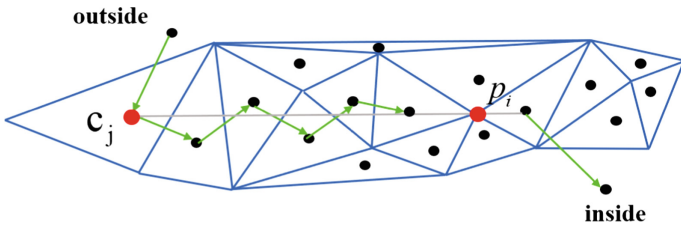tetrahedralization T. $\lambda_{visibility}$ is the size of visibility information set. $T_j(p_i)$ is

Fig. 1. The visibility conflict is the edge interested with ray $c_j p_i$, the arrowed edges
are parts of the representation of the dual graph, which weight the edge.

the credibility of the perspective, which represents the probability that vertex appears on the final surface model. Combining the Gaussian kernel function to reduce noise, the formula is as follows:

$$E_{visibility}(S) = \sum_{t \in T} \sum_{(p,c) \neq \varnothing} \lambda_{visibility}(1 - T_j(p_i)(1 - e^{\frac{-d^2}{2\sigma^2}})) \tag{2}$$

In formula (2), t is the edge in the dual graph and the intersecting triangle of the adjacent tetrahedron in the Delaunay tetrahedralization, p is the vertex in the Delaunay, c is camera center, $(p, c) \cap t$ is the ray pc intersects t, d is the distance from the intersection with p_i, σ is the standard deviation of Gaussian function. Traversing all vertexes in the Delaunay tetrahedralization, we compute the visibility term by accumulating the directed edges weights as shown in formula (2).

The surface model will be uneven while the energy equation is only computed by $E_{visibility}$. In order to reduce the influence of outliers and noise points and restore the detailed information of the surface model. Triangle t is the intersecting of adjacent Delaunay tetrahedrons. The angle between the triangle plane and the external sphere of two tetrahedrons is α, β. The representation of the angle is shown in Fig. 2. While α, β is getting smaller, the possibility of cutting edge passing through triangle t is greater, which means the possibility of the cut edge appearing on the final surface is higher. α is calculated as.

$$\cos(\alpha) = \frac{\overrightarrow{pc} \cdot \boldsymbol{n}}{|\overrightarrow{pc}| \cdot |\boldsymbol{n}|} \tag{3}$$

$\overrightarrow{pc}$ is the vector from vertex p to sphere centre c. $\boldsymbol{n}$ is the normal vector of triangle plane, E_{smooth} is computed as:

$$E_{smooth}(S) = \sum_{t \in T} 1 - min\{cos(\alpha), cos(\beta)\} \tag{4}$$

The Smooth term is computed by traversing all the edges of dual graph. The Delaunay tetrahedron is labelled as inside/outside by graph cut optimization [3]. Triangles from label outside to inside are extracted as minimum cut edges and the initial reconstructed surface result S is obtained.

4   Surface Optimization Based on Deformation Model

Details are inevitably lost when smoothing the initial surface model. In this section, initial surface model is the input, which is optimized by deformation model to achieve surface optimization. In the deformation model, we adopted photometric similarity function as date term, and the internal energy function of the active contour model is calculated as regularization item by using Laplace operator. As the internal and external energy functions are minimized globally,
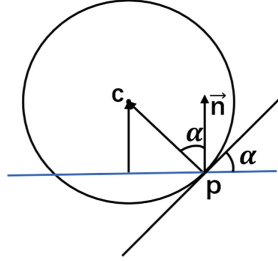
Fig. 2. It shows the 2D representation of the angle, α is the angle between triangle plane and external sphere of tetrahedrons, β is calculated the same way.

details of the surface model can be restored and a more refined surface reconstruction model can be obtained. The energy equation of the deformation model is as:

$$E(S) = E_{int}(S) + \lambda E_{ext}(S) \tag{5}$$

S is the initial surface model, λ is the weight of data item, $E_{int}(S)$ is the regularization item, which is responsible for constraining the topological structure of the surface model to prevent self-intersection and producing over smooth surface in the reconstruction process. $E_{int}(S)$ is computed by active contour model. $E_{ext}(S)$ is data item, which approximates the surface model to target model. $E_{ext}(S)$ is computed by photometric similarity function.

4.1   Data Term

The data term $E_{ext}(S)$ in the deformation model is computed by the photometric difference of images as:

$$\nabla E_{ext} = \sum_{I_i=0}^{n} \sum_{I_j=0 \cap I_i \neq I_j}^{n} \nabla M_{I_i, I_j}(S) \tag{6}$$

Matching function $M_{I_i, I_j}(S)$ is the difference between I_i and I_j, $\prod_j$ is the projection of the camera j, $\prod_{i,S}^{-1}$ is reprojecting I_i onto the surface, $I_j \circ \prod_j \circ \prod_{i,S}^{-1}$ is reprojecting the I_j onto I_i, $\Omega_{i,j}^S$ is the reprojection domain. $M_{I_i, I_j}(S)$ is as follows:

$$M_{I_i, I_j}(S) = M|_{\Omega_i \cap \Omega_{i,j}^S}(I_i, I_j \circ \prod_j \circ \prod_{i,S}^{-1}) \tag{7}$$

The data item gradient value of surface S is obtained by partial derivative of matching function with respect to variable x as:

$$\nabla M_{I_i, I_j}(S) = \int_{\Omega_i \cap \Omega_{i,j}^S} \partial M_{I_i, I_j}(x_i) DI_j(x_j) D \prod_j(x) \frac{\boldsymbol{n}^T \delta S(x)}{\boldsymbol{n}^T \boldsymbol{d_i}} \boldsymbol{d_i} dx_i \tag{8}$$

x is the reprojection 3D point of x_i, $DI_j(x_j)$ is the gradient of the image, $D\prod_j(x)$ is Jacobian matrix of $\prod_j$, $\boldsymbol{d_i}$ is the vector representing the camera i and the point x, $\boldsymbol{n}$ is the normal vector of 3D points.

4.2   Photometric Similarity Function

Matching function $M_{I,J}(S)$ is constructed by $L_{I,J}(x)$ on the basis of the local dependency between image I and image J.

$$M(I,J) = \int_{\Omega_i \cap \Omega_{i,j}^S} 1 - L_{I,J}(x_i)dx \tag{9}$$

$L_{I,J}(x)$ is photometric similarity function of image I and J at pixel x, $\Omega_{i,j}^S$ is the reprojection domain. In I_i, w_i is $n \times n$ pixel block centered on x_i, w_j is $n \times n$ pixel block centered on x_j. g_i is the grayscale value at pixel x_i, σ_g is the color standard deviation, σ_x is the distance standard deviation.

$$L_{I,J}(x_i) = \frac{cov(w_i, w_j)}{\sqrt{cov(w_i)cov(w_j, w_j)}} \tag{10}$$

$$E(x) = \frac{\sum_m^{n \times n} w_m x_m}{\sum_m^{n \times n} w_m} \tag{11}$$

$$w_m = e^{\left(-\frac{|g_m - g_i|^2}{2\sigma_g^2} + \frac{|x_m - x_i|^2}{2\sigma_x^2}\right)} \tag{12}$$

4.3   Regularization Term

The regularization term is constructed by the internal function of the active contour models to prevent the self-intersection or producing over smooth of the surface model. We simplify the weight, λ_1 is the elasticity, λ_2 is the intensity coefficient to control the curves degree of surface, which ultimately makes the curvature of the surface tend to be stable. The minimum of energy function for equation is solved by Euler-Lagrange theorem as:

$$\nabla E_{int}(S) == \lambda_1 \triangle S - \lambda_2 \triangle^2 S \tag{13}$$

Δ is the laplace operator, Δ^2 is the biharmonic Operator. For each vertex v in the surface S, the laplace operator is computed as formula (14), $N(v)$ is a set of 1-ring nearest vertices of v. n is the number of $N(v)$. The gradient of v is as:

$$\triangle v = \left(\sum_{i \in N(v)} \left(\frac{v_i}{n}\right) \right) - v \tag{14}$$

$\triangle^2 v$ is calculated as:

$$\triangle^2 v = \sum_{i \in N(v)} \left(\frac{\triangle v_i}{n}\right) - \triangle v \tag{15}$$

For all vertices v of the surface, the $\nabla E_{int}(v)$ is accumulated by $\nabla E_{int}(S)$, as shown in formula (16):

$$\nabla E_{int}(S) = \sum_{v \in S} \nabla E_{int}(v) \tag{16}$$

4.4   Optimizing of the Final Surface

Finally, the surface is optimized by formula (5), and the discrete form of formula (5) is shown in formula (17). After several iterations of all vertices on the surface by gradient descent, surface model is approximated to the real surface of the object.

$$S^{k+1} = S^k + \triangle t(\nabla E_{int}(S) + \lambda \nabla E_{ext}(S)) \tag{17}$$

λ is the weight of data term, $\triangle t$ is the incremental step. All vertices v are iterated until the whole surface model converges. Finally, the reconstructed surface model is obtained.

5   Experiments

In this section, experiments are divided into two parts. To confirm the effectiveness of our method, we tested on four standard datasets [18]: Castle-Entry, Castle, Fountain and Herzjesu, and compared the experimental results with PSR [10] and FSSR [5]. Moreover, in order to verify the accuracy of our approach, we compared the reconstructed surface models with real three-dimensional models, and have experimented our method and GDMR on four datasets [18] to evaluate the similarity between the experiment results and ground truth of models.

In experiments, bundle system [16,17] is adopted to obtain the initial 3D point cloud, and then we process the point cloud by PMVS [6], which is used as the input of the surface reconstruction. In the proposed approach, we get the initial reconstruction surface with parameter $\sigma = l/2$, where l represents the median of Delaunay side length, after that we optimize the surface by deformation model, and set threshold $n = 4$, we weight $\lambda_1 = 0.8$, $\lambda_2 = 0.2$ in optimation energy formulation, the weight factor λ of the iteration equation is set $\lambda = 0.5$, step $\triangle t$ at each iterations is set $\triangle t = 0.5$, which is reduced by 0.02 times after each iteration.

For the qualitative evaluation, we conducted on the four standard datasets [18] compared with PSR [10] and FSSR [5]. PSR is experimented at a depth of 11. Octree depth of FSSR is set to 10. As illustrated in Fig. 3, we can see that in the easily occluded areas such as pillars of the Herzjesu, our method reconstruct the surface with more details. In areas with uneven distribution of samples such as windows of the Herzjesu, our method reconstruct smoother wall than the others. In Fig. 4, surface details of spiral sculpture of the Fountain are more accurate and closer to the real model. In Fig. 5, the pillar and edge of Castle-entry are more detailed, while the reconstructed surfaces of PSR and FSSR are smoother and image details are lost. In Fig. 6, the reconstruction results of Castle show

that the proposed algorithm is superior to PSR [10] and FSSR [5] in terms of detail recovery and reconstruction integrity.

Figures 3, 4, 5 and 6 demonstrate that our method increases the local details information of reconstructed surface, and it can be found that PSR [10] and FSSR [5] are vulnerable to a large number of noise points and outliers, resulting in poor reconstruction effect. Our method improves the precision of the surface reconstruction due to decomposing the surface model, and obtains accurate surface reconstruction by optimizing the surface details through the deformation model.
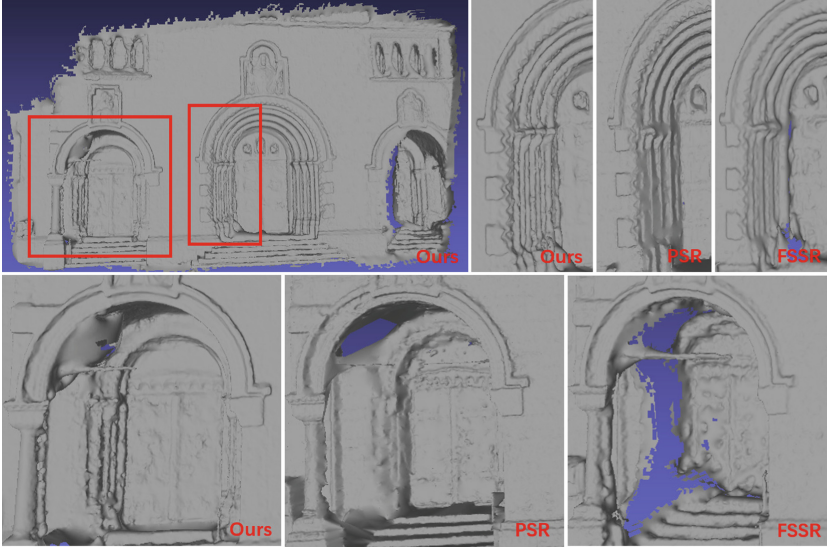

Fig. 3. The reconstruction result experimented on Herzjesu shows that the door and door frame reconstructed by the proposed method is more clearly than the other methods [5,10].

For the quantitative evaluation, we compared the reconstructed surface model and GDMR [19] with the real three-dimensional model respectively. We adopted the four standard datasets [18] as the assessment model. Table 1 and Table 2 show the error statistics of the surface model reconstructed by the algorithm and the ground truth on the Fountain and Herzjesu, and the error statistics of the GDMR and ground truth. In Table 1, the accuracy of the model after optimization of the deformation model in this paper is reduced when the error is 0.1. In Table 2, When the error is 0.045 and 0.06, the accuracy of the model is reduced, which is because the partial occlusion area increases the number of vertices and triangles of the occlusion area by triangulation during the deformation optimization process, resulting in an increase in the number of error points and optimization. In addition, from Table 1 and Table 2, it can be seen that the accuracy of the algorithm in this paper is better than that of GDMR. The initial
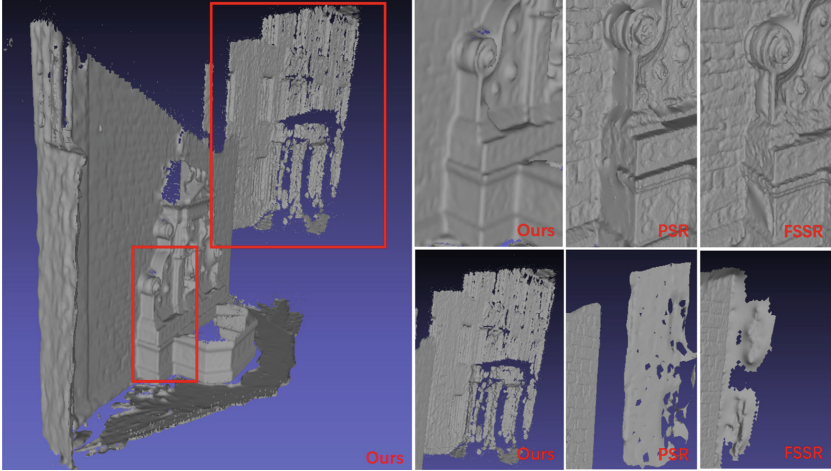
Fig. 4. The reconstruction result experimented on Fountain shows that outline of the statue and the wall reconstructed by the proposed method is more complete than the other methods [5, 10].
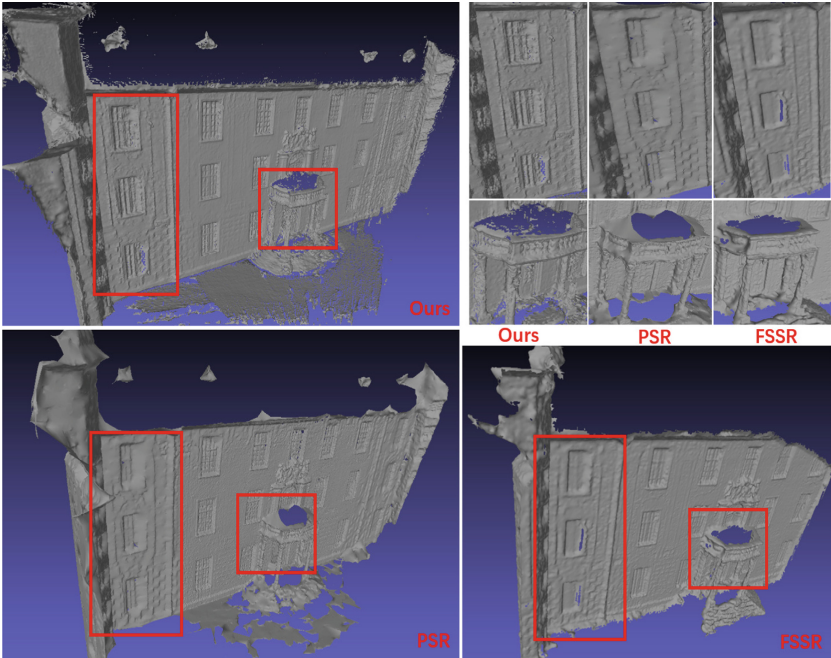

Fig. 5. The reconstruction result experimented on Castle-entry shows that the outline of the castle is clearer, and pillars is more complete than the other methods [5, 10].
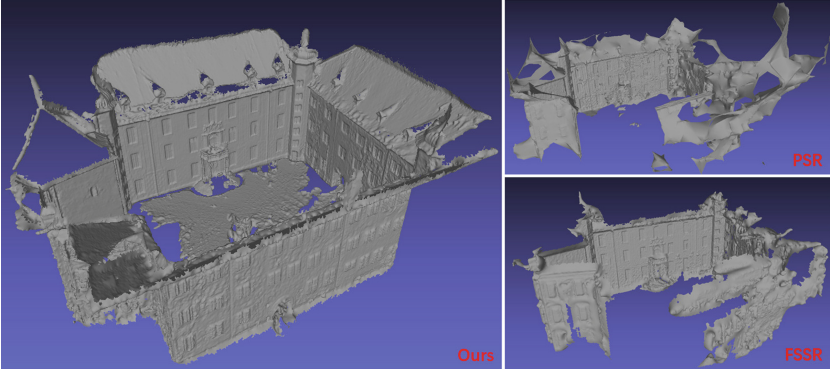
Fig. 6. The reconstruction result experimented on Castle shows that the completeness and detail of our approach is reconstructed better than the other methods [5,10].

Table 1. Relative errors between reconstructed results of our approach, GDMR [19] and the Fountain ground truth.

ratio(%) \ error(m) surface model	0.02	0.04	0.06	0.80	0.10
the initial surface	78.415	96.24	98.235	98.686	99.572
optimization surface	78.552	96.657	98.268	98.841	99.361
GDMR	76.436	95.985	98.379	98.794	99.358

Table 2. Relative errors between reconstructed results of our approach, GDMR [19] and the Herzjesu ground truth.

ratio(%) \ error(m) surface model	0.015	0.030	0.045	0.060	0.075
the initial surface	93.068	97.489	98.985	99.681	99.868
optimization surface	94.585	97.337	98.151	98.538	99.746
GDMR	94.385	97.364	98.086	98.479	99.685

model, deformation optimization model of our method and GDMR are quantitatively analyzed by experiments. The experiments show that our algorithm achieves higher accuracy than GDMR [19].

6   Conclusion

In this paper, we presented an approach of 3D surface reconstruction based on Delaunay triangulation. The initial surface model is derived by Delaunay trian-

gulation and graph-cut optimization. Then we optimized the initial surface by deformation model and gradient descent to obtain the final surface. We experimented on four standard datasets of Castle-Entry, Castle, Fountain and Herzjesu. The proposed approach could reconstruct high quality three-dimensional surface models of object from the point cloud models with lots of noise and complex topological structures.

References

1. Bai, R., Qu, Y.: Study on three-dimensional visual simulation technology and its application in surface coal mine. In: 2012 Fourth International Conference on Computational and Information Sciences, pp. 14–16. IEEE (2012)
2. Berger, M., et al.: State of the art in surface reconstruction from point clouds. In: EUROGRAPHICS Star Reports, vol. 1, pp. 161–185 (2014)
3. Boykov, Y., Kolmogorov, V.: An experimental comparison of min-cut/max-flow algorithms for energy minimization in vision. IEEE Trans. Pattern Anal. Mach. Intell. **9**, 1124–1137 (2004)
4. Bruno, F., Bruno, S., De Sensi, G., Luchi, M.L., Mancuso, S., Muzzupappa, M.: From 3D reconstruction to virtual reality: a complete methodology for digital archaeological exhibition. J. Cult. Heritage **11**(1), 42–49 (2010)
5. Fuhrmann, S., Goesele, M.: Floating scale surface reconstruction. ACM Trans. Graph. (ToG) **33**(4), 46 (2014)
6. Furukawa, Y., Ponce, J.: Accurate, dense, and robust multiview stereopsis. IEEE Trans. Pattern Anal. Mach. Intell. **32**(8), 1362–1376 (2009)
7. Hafeez, J., Lee, S., Kwon, S., Hamacher, A.: Image based 3D reconstruction of texture-less objects for VR contents. Int. J. Adv. Smart Converg **6**(1), 9–17 (2017)
8. Jancosek, M., Pajdla, T.: Multi-view reconstruction preserving weakly-supported surfaces. In: CVPR 2011, pp. 3121–3128. IEEE (2011)
9. Kazhdan, M., Bolitho, M., Hoppe, H.: Poisson surface reconstruction. In: Proceedings of the Fourth Eurographics Symposium on Geometry Processing, vol. 7 (2006)
10. Kazhdan, M., Hoppe, H.: Screened poisson surface reconstruction. ACM Trans. Graph. (ToG) **32**(3), 29 (2013)
11. Labatut, P., Pons, J.P., Keriven, R.: Robust and efficient surface reconstruction from range data. In: Computer Graphics Forum, vol. 28, pp. 2275–2290. Wiley Online Library (2009)
12. Labatut, P., Pons, J.P., Keriven, R.: Efficient multi-view reconstruction of large-scale scenes using interest points, delaunay triangulation and graph cuts. In: 2007 IEEE 11th International Conference on Computer Vision, pp. 1–8. IEEE (2007)
13. Laurentini, A.: The visual hull concept for silhouette-based image understanding. IEEE Trans. Pattern Anal. Mach. Intell. **16**(2), 150–162 (1994)
14. Mostegel, C., Prettenthaler, R., Fraundorfer, F., Bischof, H.: Scalable surface reconstruction from point clouds with extreme scale and density diversity. In: Proceedings of the IEEE Conference on Computer Vision and Pattern Recognition, pp. 904–913 (2017)
15. Pan, Q., Reitmayr, G., Drummond, T.: Proforma: probabilistic feature-based online rapid model acquisition. In: BMVC, vol. 2, p. 6. Citeseer (2009)
16. Snavely, N., Seitz, S.M., Szeliski, R.: Photo tourism: exploring photo collections in 3D. In: ACM transactions on graphics (TOG), vol. 25, pp. 835–846. ACM (2006)

17. Snavely, N., Seitz, S.M., Szeliski, R.: Modeling the world from internet photo collections. Int. J. Comput. Vision **80**(2), 189–210 (2008)
18. Strecha, C., Von Hansen, W., Van Gool, L., Fua, P., Thoennessen, U.: On benchmarking camera calibration and multi-view stereo for high resolution imagery. In: 2008 IEEE Conference on Computer Vision and Pattern Recognition, pp. 1–8. IEEE (2008)
19. Ummenhofer, B., Brox, T.: Global, dense multiscale reconstruction for a billion points. In: Proceedings of the IEEE International Conference on Computer Vision, pp. 1341–1349 (2015)
20. Wang, J., Yang, Z., Jin, L., Deng, J., Chen, F.: Parallel and adaptive surface reconstruction based on implicit pht-splines. Comput. Aided Geom. Des. **28**(8), 463–474 (2011)
21. Wei, Z., Qi, G., Qiang, Z., Wang, Y., Jian, O.: A non-contact measurement method of cabin capacity based on structured light vision. In: IEEE International Conference on Mechatronics & Automation (2016)
22. Wu, H.N., Sun, X.R., Liu, W.J.: Research on 3D modeling technology of battlefield environment. Appl. Mech. Mater. **651–653**, 2020–2023 (2014)
23. Xie, A., Fang, C., Huang, Y., Fan, Y., Pan, J., Peng, F.: Application of three-dimensional reconstruction and visible simulation technique in reoperation of hepatolithiasis. J. Gastroenterol. Hepatol. **28**(2), 248–254 (2013)